

## Instantaneous crack detection under varying temperature and static loading conditions

Yun-Kyu An<sup>†</sup> and Hoon Sohn<sup>\*,†,§</sup>

*The Department of Civil and Environmental Engineering, KAIST, Daejeon 305-701, South Korea*

### SUMMARY

On the basis of guided wave propagation in plate-like structures, the authors' group previously developed a reference-free crack detection technique. The previous technique requires the placement of two pairs of collocated lead zirconate titanate (PZT) transducers on the top and bottom surfaces of a structure. However, as access to both surfaces can be limited for some structural systems, such as aircraft and pipelines, an improved reference-free crack detection technique is developed in this study to overcome this limitation. The major advancements of the proposed reference-free technique over the previous one are (1) reformulation of the reference-free technique considering energy distribution among Lamb wave modes to overcome the limitations of the previous time domain approach, (2) extension to allow the use of various input waveforms including broadband chirp signals and narrowband toneburst signals, and (3) newly designed PZT transducers for single surface installation and better ruggedness. Numerical simulations and experimental tests on aluminum plates are performed to investigate the performance of the proposed technique. In particular, its robustness to varying temperature and external loading is experimentally tested. Copyright © 2010 John Wiley & Sons, Ltd.

**KEY WORDS:** guided wave propagation; structural health monitoring; reference-free crack detection; instantaneous damage diagnosis; loading and temperature variations

### 1. INTRODUCTION

Guided wave-based techniques have become popular Structural Health Monitoring (SHM) and Nondestructive Testing approaches because guided waves are sensitive to small defects and are capable of propagating over a long distance with little attenuation [1–3]. Previously developed

---

\*Correspondence to: Hoon Sohn, The Department of Civil and Environmental Engineering, KAIST, Daejeon 305-701, South Korea.

<sup>†</sup>E-mail: hoonsohn@kaist.ac.kr

<sup>‡</sup>Ph.D. Student.

<sup>§</sup>Associate Professor.

Contract/grant sponsor: Ministry of Education, Science and Technology (MEST)

guided wave-based SHM techniques for aerospace, civil, and mechanical engineering have focused on detecting changes from the baseline data obtained from pristine conditions of a structure [4,5]. However, there are significant technical challenges to realizing this pattern comparison. Because operational and environmental variations of the system can cause signal changes, the simple pattern comparison with the baseline data can produce false alarms [6].

To overcome this limitation, a reference-free damage detection technique, an approach that identifies damage without comparing the current data with the baseline data obtained from the pristine condition of the structure being monitored, was previously developed by the authors' group [7]. The previous technique detected crack-induced mode conversion in plate-like structures using two pairs of collocated lead zirconate titanate (PZT) transducers placed on both surfaces of the structures. However, access to both surfaces of a structure is often limited for applications, such as aircrafts and pipelines. To tackle this issue, another reference-free technique that requires the placement of newly designed PZT transducers only on a single surface was developed in the time domain [8]. This time domain approach has its own drawbacks. When multiple reflections and higher Lamb wave modes appear, the interpretation of the time response signal becomes a challenging task, demanding advanced signal processing. Furthermore, the time domain analysis requires careful tuning of design parameters, such as the driving frequency, the type of the input waveform, and the signal duration to name a few.

In this study, the reference-free SHM technique is further advanced to tackle the aforementioned technical challenges. First, the reference-free technique is reformulated, considering energy distributions among Lamb wave modes to overcome the limitations of the previous time domain approach. Second, the data acquisition time has been significantly reduced by allowing the use of various input waveforms, such as narrowband toneburst signals and broadband chirp signals. Finally, the robustness of the improved reference-free technique to varying temperature and external loading has been experimentally validated.

This study is organized as follows. First, the theoretical development of the proposed crack detection technique is described in Section 2. Then, numerical simulations are executed to validate some of the assumptions made during the theoretical development. Finally, experimental studies under varying temperature and external static loading are conducted to validate the robustness of the developed technique under changing environmental and operational conditions.

## 2. THEORETICAL DEVELOPMENT

### 2.1. Development of a dual-PZT

The previous reference-free technique isolated the mode conversion produced by crack formation using two pairs of collocated PZT transducers. In this study, it was necessary to collocate two identical PZT transducers on top and bottom surfaces of the structure. However, often access to both surfaces of a structure can be limited, and it can be difficult to precisely place two PZTs at the same position but on the opposite sides. To overcome this limitation, a new PZT design coined 'dual-PZT' is developed, as shown in Figure 1(a) [8]. The dual-PZT is divided into inner circle and outer ring parts. These segmentations of the dual-PZT allow excitation and sensing of guided waves using the inner circle, the outer ring, or the both parts simultaneously. It will be shown in Section 2.2 as how this selective guided wave actuation and

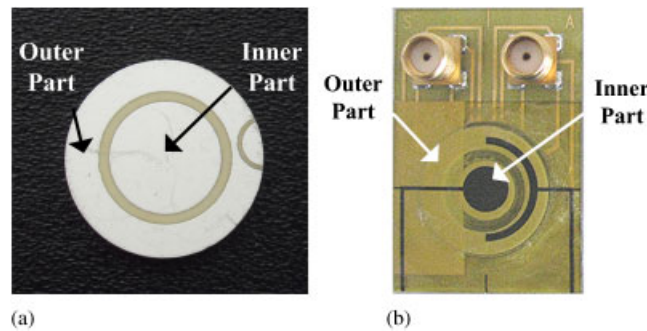


Figure 1. Design of dual-PZT transducers: (a) Raw dual-PZT and (b) Packed dual-PZT.

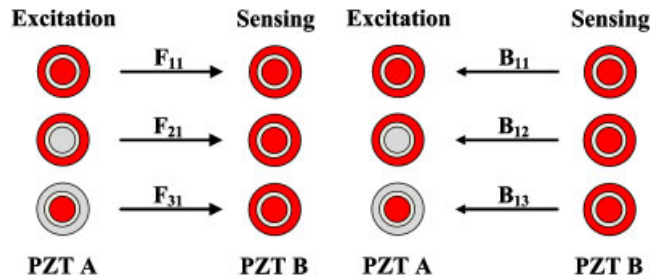


Figure 2. The notations of the signals measured from a pair of dual-PZTs: ‘*F*’ denotes a forward signal excited by PZT A and measured by PZT B. ‘*B*’ represents a backward signal propagating in the opposite direction. The ‘1’, ‘2’, and ‘3’ of  $F_{ij}$  and  $B_{ij}$  represent the entire PZT area, the outer ring part and the inner circle part of a dual-PZT, respectively. The darker area of a PZT denotes the PZT area used for PZT excitation or sensing.

sensing using different PZT sizes can be applied to the isolation of mode conversion signals induced by a crack.

For field deployments, the ruggedness of the PZT transducer is critical because the PZT transducer itself can be the weakest link in the entire SHM system. In this study, a new packed dual-PZT shown in Figure 1(b) is developed so that the bare PZT can be encapsulated using a Kapton tape with printed circuits. This packed PZT design makes the PZT installation easier, achieves a reliable wire connection and insulates the ground of the PZT transducer from the host structure, minimizing electromagnetic interference. This dual-PZT is manufactured by Metis Design Corporation [9].

Next, the notations used to describe the time signals measured from a pair of dual-PZTs are introduced. In Figure 2, ‘*F*’ denotes a forward signal excited by a left PZT (PZT A) and measured by the other PZT (PZT B) on the right side. ‘*B*’ represents a backward signal propagating in the opposite direction. The subscripts ‘1’, ‘2’, and ‘3’ represent the entire area, the outer ring part, and the inner circle part of a dual-PZT, respectively. In Figure 2, the darker area of a PZT denotes the PZT area activated for PZT excitation or sensing. For example,  $F_{31}$  represents the forward signal excited by the inner circle part of PZT A and measured by the whole area of PZT B.

## 2.2. Extraction of mode conversion

Lamb waves can propagate in two types of modes, symmetric ( $S$ ) and anti-symmetric ( $A$ ) modes [10]. When Lamb waves propagating along a plate-like structure encounter a geometrical discontinuity such as a crack on the structure, portion of a Lamb wave mode is transformed into the other mode. This phenomenon is defined as mode conversion [11]. For example, when a  $S_0$  mode passes through a crack, part of the transmitted  $S_0$  mode is converted into an  $A_0$  mode ( $A_0/S_0$ ) and the rest remain unchanged ( $S_0/S_0$ ). Similarly, some portion of  $A_0$  mode can be converted into an  $S_0$  mode ( $S_0/A_0$ ) and the others are unchanged ( $A_0/A_0$ ) due to a crack formation.

In this study, it is explained how converted Lamb wave signals can be extracted from the various signals measured by a pair of dual-PZTs. The basic premise is that, when PZTs with different sizes are used for measuring  $F_{ij}$  and  $B_{ij}$  ( $ij$ ), converted modes ( $A_0/S_0$  and  $S_0/A_0$ ) appear in  $D_{ij}$  ( $= F_{ij} - B_{ij}$ ) only when damage exists [8]. For example, Figure 3(a) shows that  $F_{13}$  and  $B_{13}$  are identical in the time domain when there is no damage. Therefore, the difference  $D_{13}$  ( $= F_{13} - B_{13}$ ) becomes a null signal. On the other hand, converted modes,  $A_0/S_0$  and  $S_0/A_0$ , appear in  $F_{13}$  and  $B_{13}$  of Figure 3(b) when crack is formed. In this study,  $A_0/S_0$  in  $F_{ij}$  is identical to  $S_0/A_0$  in  $B_{ij}$  (not to  $A_0/S_0$  in  $B_{ij}$ ), and  $S_0/A_0$  in  $F_{ij}$  is reciprocal to  $A_0/S_0$  in  $B_{ij}$  [8]. Note that  $A_0/S_0$  in  $F_{ij}$  exactly matches with  $A_0/S_0$  in  $B_{ij}$  only when the size of the exciting PZT is same as that of the sensing PZT ( $i = j$ ). Therefore, converted modes can be isolated by subtracting  $B_{ij}$  from  $F_{ij}$ , and the extracted mode conversion appears in  $D_{ij}$ . In this study, a total of six different  $D_{ij}$  signals can be constructed from six different pairs of  $i$  and  $j$ . Note that signals  $F_{ij}$  and  $B_{ij}$  are defined as pair signals in this study. The subsequent damage classifier will be built on these extracted mode conversion signals.

## 2.3. Superposition relationships among measured signals

Various error sources, such as PZT imperfection, variation of PZT sizes, and bonding conditions, can all contribute to the deviation of superposition relationships. In this study, superposition relationships among measured signals are exploited to establish the necessary threshold value for the damage classification introduced in subsection 2.4. Figure 4 illustrates two types of the superposition relationships among the signals measured from a pair of dual-PZTs. The first superposition relationship is concerned with the variation of the exciting PZT size as shown in Figure 4(a). It shows the summation of the response signals obtained by the outer ring excitation ( $F_{2j}$ ) and the inner circle actuation ( $F_{3j}$ ) is equal to the response

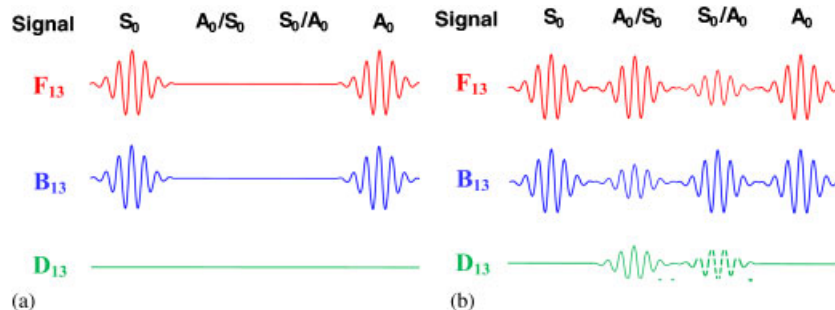


Figure 3. Extraction of mode conversion in the time domain: (a) There is no difference between  $F_{13}$  and  $B_{13}$  signals without damage and (b) mode conversion appears in signal  $D_{13}$  ( $= F_{13} - B_{13}$ ) with damage.

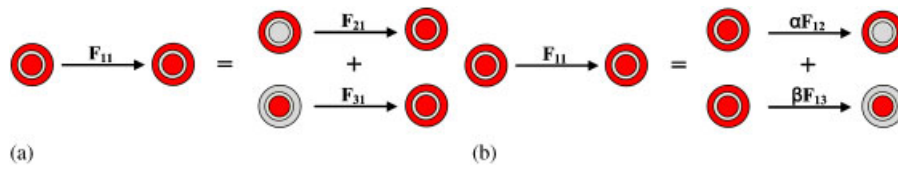


Figure 4. Superposition relationships among time signals measured from a pair of dual-PZTs: (a) Superposition relationships among signals measured with varying excitation PZT sizes and (b) Superposition relationships among signals measured with varying sensing PZT sizes (Note that only the darker areas are activated for guided wave excitation and sensing.).

corresponding to the whole area PZT excitation ( $F_{1j}$ ) for any fixed sensing PZT size,  $j$  [12].

$$F_{1j} = F_{2j} + F_{3j} \quad \text{for } j = 1 \sim 3 \quad (1)$$

Next, the other superposition relationship for varying sensing PZT size is established. In terms of sensing, the output voltage of a sensing PZT is proportional to the size of the PZT [13]. Consequently, the response signal measured by the whole PZT area becomes identical to the weight sum of the responses obtained by the outer ring and the inner circle parts regardless of the size of the exciting PZT.

$$F_{i1} = \alpha F_{i2} + \beta F_{i3} \quad \text{for } i = 1 \sim 3 \quad (2)$$

where  $\alpha + \beta = 1$ , and  $\alpha$  and  $\beta$  values are the ratios of the outer and inner PZT sizes to the whole PZT size, respectively. For instance, if the sizes of the outer and inner parts are identical, both  $\alpha$  and  $\beta$  become 0.5. Note that all superposition relationships described in this study are also valid for backward signals and regardless of the presence of damage.

#### 2.4. Reference-free damage classification

In this section, a reference-free damage classifier that operates on the extracted mode conversion signals is developed. The energy level of the crack-induced mode conversion is computed by transferring the mode conversion signals in the time domain into the frequency domain. Then, a threshold value is calculated from the energy level of the error signals that stem from the imperfect matching of the aforementioned superposition relationships. Finally, when the energy level of the mode conversion exceeds the error energy level, the structure is adjudged damaged.

First, the mode conversion energy (MCE) is computed from the mode conversion time signals described in Section 2.2: (1) The mode conversion time signal  $D_{ij}$  ( $= F_{ij} - B_{ij}$ ) is extracted at a specific driving frequency; (2)  $D_{ij}$  is converted to the frequency domain using the Fast Fourier Transform (FFT); (3) The previous two steps are repeated over the entire frequency range of interest; (4) MCE is defined as the summation of the magnitude of  $D_{ij}$  in the frequency domain over the entire frequency range.

$$\text{MCE}_{ij} = \frac{2E(D_{ij})}{E(F_{ij}) + E(B_{ij})} \quad \text{for } i \neq j \quad (3)$$

where  $E(D_{ij})$  denotes the FFT of  $D_{ij}$  over the entire frequency range investigated ( $E(D_{ij}) = \int \text{FFT}(D_{ij}) df$ ). Note that the MCE is normalized by the energy levels of  $F_{ij}$  and  $B_{ij}$ , and a total of six MCE values can be obtained. Finally, the averaged MCE (AMCE) is defined as the average of these six MCE values and this value is used for the subsequent damage classification.

Second, the normalized energy levels of the errors inherent in the superposition relationships described in Section 2.3 are computed in a manner similar to the computation of MCE.

$$\text{FAE}_{1j} = \frac{2E(F_{1j} - F_{2j} - F_{3j})}{E(F_{1j}) + E(F_{2j} + F_{3j})} \quad \text{for } j = 1 \sim 3 \quad (4)$$

$$\text{FSE}_{i1} = \frac{2E(F_{i1} - \alpha F_{i2} - \beta F_{i3})}{E(F_{i1}) + E(\alpha F_{i2} + \beta F_{i3})} \quad \text{for } i = 1 \sim 3 \quad (5)$$

where the first three error energy levels,  $\text{FAE}_{1j}$ , are computed from the excitation superposition relationships of  $F_{ij}$  signals, and the last three are from the sensing superposition relationships. Additional six error energy levels can be also computed from  $B_{ij}$  signals, producing a total of 12 error energy levels.

Finally, an instantaneous reference-free damage classifier is established. The threshold value is established from the previously computed 12 error energy levels using extreme value statistics [14]. A Weibull distribution is fit to the error energy levels, and the threshold is set in accordance to a one-sided 95.4% confidence interval. Damage is alarmed when AMCE exceeds the threshold value. Otherwise, the structure is diagnosed undamaged.

### 3. NUMERICAL SIMULATION

The proposed technique for crack detection was first validated through 2-D numerical simulations, using the plain strain assumption. The simulations were performed using COMSOL 3.3a Multi-physics software with the mapped mesh (1 mm  $\times$  1 mm maximum size), the sampling rate of 4 MS/s, the mass damping coefficient of  $10^{-4}$ , the absolute tolerance of  $10^{-11}$  and the second order Max. BDF [15]. An aluminum plate, that is 70 cm long and 6 mm thick, is used for numerical simulation. For the damaged case, a 3-mm deep and a 1-mm wide notch was introduced 100 mm away from PZT A, as shown in Figure 5(a). Two identical dual-PZTs were placed on the top surface of the plate as shown in Figure 5(b). PSI-5AE type PZTs were used for the simulations. In this study, the thickness and the diameters of the inner and outer PZTs were 0.508, 10, and 18 mm, respectively. A narrowband toneburst signal at 150 kHz was used as an input signal. Note that the numerical simulations using chirp input signals from 100 to 200 kHz are also performed, and successful damage diagnosis has been achieved.

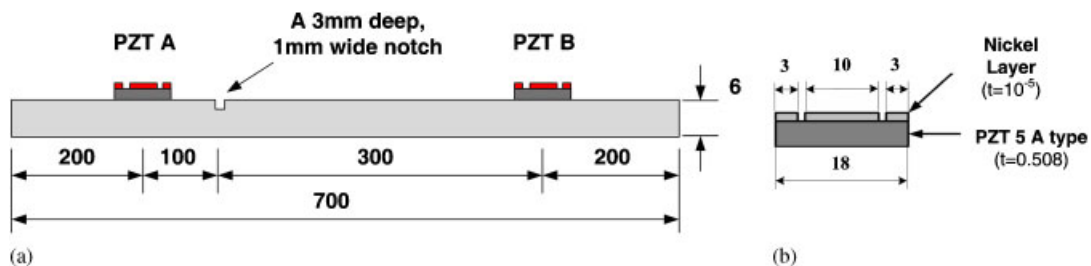


Figure 5. Numerical simulation setup: (a) specimen and (b) dual-PZT transducer (All dimensions are in millimeter).

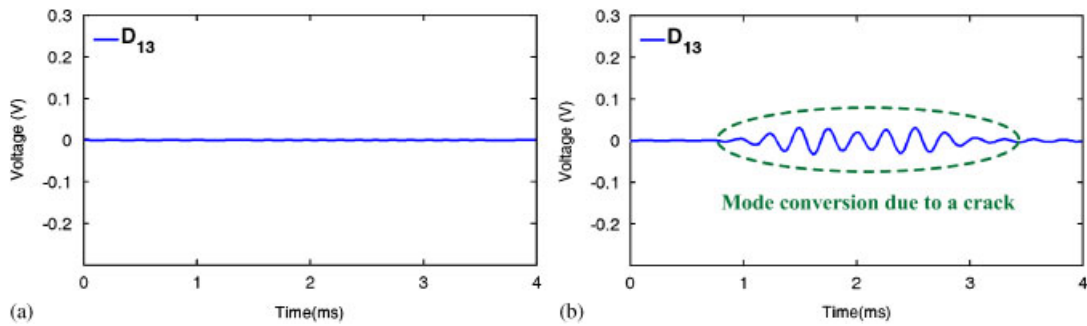


Figure 6. Extraction of mode conversion signal  $D_{13}$  ( $= F_{13} - B_{13}$ ) obtained from simulation at 150 kHz: (a) Intact case and (b) Damaged case.

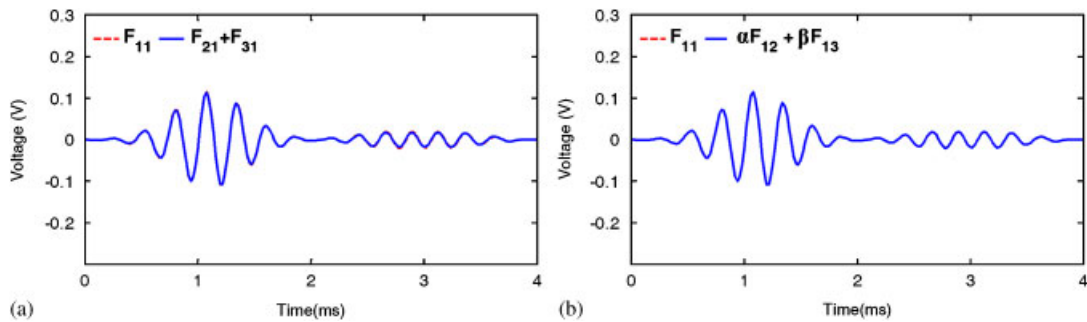


Figure 7. Numerical verification of the superposition relationships described in Equations (1) and (2): (a) Varying exciting PZT sizes ( $F_{11} = F_{21} + F_{31}$ ) and (b) Varying sensing PZT sizes ( $F_{11} = \alpha F_{12} + \beta F_{13}$ ).

### 3.1. Extraction of mode conversions in the time domain

Figure 6(a) shows that no mode conversion appears in  $D_{13}$  ( $= F_{13} - B_{13}$ ), when  $F_{13}$  and  $B_{13}$  were obtained from the intact condition of the plate. On the other hand, the mode conversion clearly appeared when the notch was introduced. Similar results were obtained as long as different PZT sizes were used for excitation and sensing.

### 3.2. Superposition relationships among measured signals in the time domain

In this study, the superposition relationships described in Equations (1) and (2) were verified through numerical simulations. Figure 7(a) and (b) shows the superposition relationships with varying exciting and sensing PZT sizes obtained from the intact condition, respectively. Note that  $\alpha$  and  $\beta$  coefficients were calculated to be 0.643 and 0.357, respectively, based on the PZT dimensions shown in Figure 5(b). These superposition relations were also verified for different PZT pairs and the damage case although they were not reported here due to the space limit.

## 4. EXPERIMENTAL VERIFICATION

The effectiveness of the proposed reference-free crack detection technique was examined through laboratory experiments conducted on aluminum plates with the dimensions of



610 mm  $\times$  400 mm  $\times$  6 mm. The overall test setup and the test specimen are shown in Figure 8. The data acquisition system consisted of an arbitrary waveform generator (AWG), a high-speed signal digitizer (DIG), a low noise preamplifier, and multiplexers. Using the 16-bits AWG, toneburst and chirp input signals with a  $\pm 10$  peak-to-peak voltage were generated. To compute the mode conversion and error energies, a driving frequency range of 100–150 kHz with 10 kHz increment was used for both the toneburst and chirp input signals. The output voltage was measured by the 14-bits DIG. Then, the response signals were measured 10 times and averaged in the time domain to improve the signal-to-noise ratio. In addition, a bandpass filter with 1-kHz and 1-MHz cutoff frequencies was used.

Newly designed dual-PZT patches described in Figure 1(b) were mounted on one side of the specimen as shown in Figure 8. The thickness and the diameters of the inner and outer PZTs were 0.508, 8, and 18 mm, respectively. Investigated damage cases are shown in Figure 9. In damage case I, a notch was introduced between PZTs A and B, but a notch was placed out of the direct wave propagation path for damage case II.

#### 4.1. Instantaneous damage classification

The damage classification was performed on the AMCE values obtained using toneburst input signals. Figure 10 shows that the threshold value was greater than AMCE for the intact case. Then, the AMCE value exceeded the threshold value for all the subsequent damage cases. Similar results were observed when chirp input signals were used instead of the toneburst signals as reported in Figure 11. Based on the numerical and experimental analyses, the advantages of the broadband excitations are clearly demonstrated. Using the broadband excitations, the data acquisition and computation times can be significantly reduced, the amount of data that has to be processed and stored can be minimized, and a precise tuning of the excitation frequency becomes unnecessary.

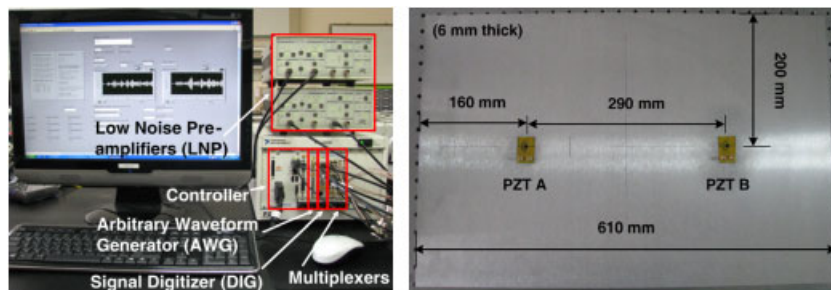


Figure 8. Experimental setup and test specimen.

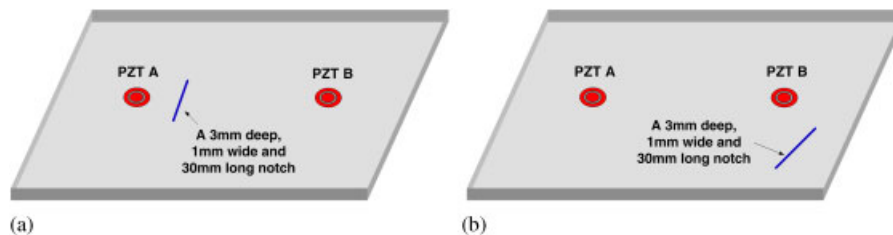


Figure 9. Experimentally investigated damaged cases: (a) Damage case I and (b) Damage case II.



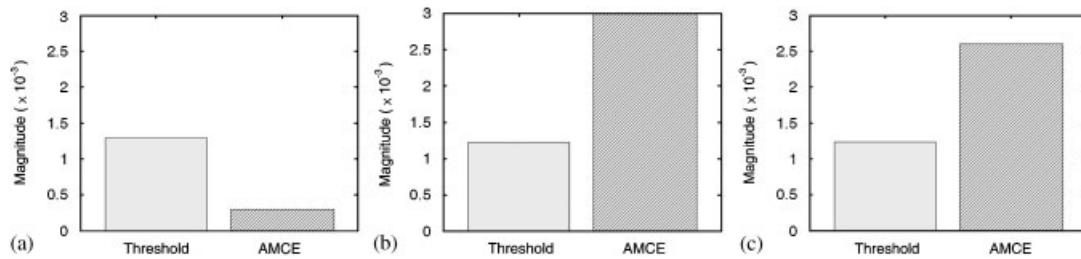


Figure 10. Reference-free damage classification using toneburst input waveforms: (a) Intact case, (b) Damage case I and (c) Damage case II (Note that Threshold and AMCE denote the instantaneous threshold value obtained from error energy and the AMCE, respectively. The structure is adjudged damaged when AMCE exceeds Threshold.).

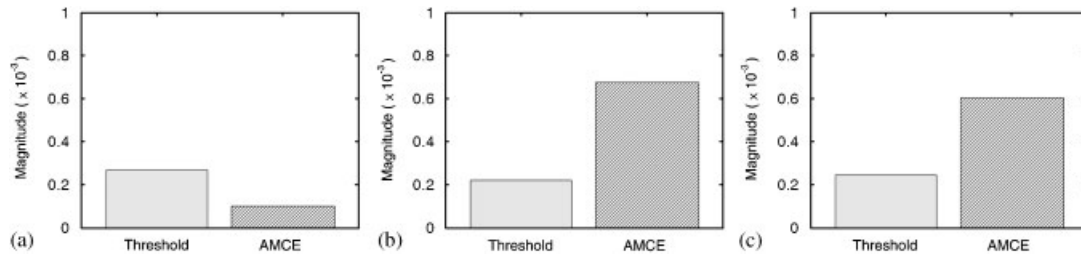


Figure 11. Reference-free damage classification using chirp input waveforms: (a) Intact case, (b) Damage case I and (c) Damage case II (Note that Threshold and AMCE denote the instantaneous threshold value obtained from error energy and the AMCE, respectively. The structure is adjudged damaged when AMCE exceeds Threshold.).

#### 4.2. The effect of temperature and static loading variations

In this section, the robustness of the proposed technique under changing temperature and loading conditions is investigated. In reality, dynamic loading effects can be readily alleviated using time domain averaging and filtering techniques [16]. In this study, strain-induced three-point static loading tests were performed so that the robustness of the proposed technique to strain variations. Figure 12 shows the temperature chamber and universal test machine (UTM) used in this study. All the other experimental setups and the investigated damage cases are same as the previous ones in Section 4.1 unless noted differently.

The temperature chamber can control both temperature and humidity. For the temperature experiment presented in this study, damage diagnosis was conducted at  $-30$ ,  $0$ ,  $20$  and  $50^\circ\text{C}$  with 30% humidity above  $0^\circ\text{C}$ . In addition, a thermocouple was used to measure the temperature of the specimen's surface within the temperature chamber.

Figure 13(a) shows the mode conversion signal  $D_{13}$ , obtained from different temperature conditions of damage case I. Although the mode conversion appears at all temperatures, the phase and amplitude of the mode conversion signal changed. In spite of these temperature-induced variations of the time signals, Table I shows that the proposed damage classifier correctly detected the two damage cases under varying temperature.

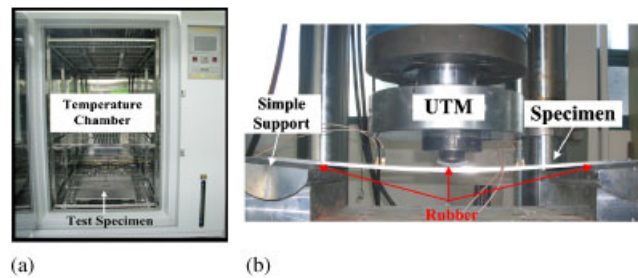


Figure 12. Experimental setups for temperature and loading tests: (a) Temperature chamber and (b) UTM.

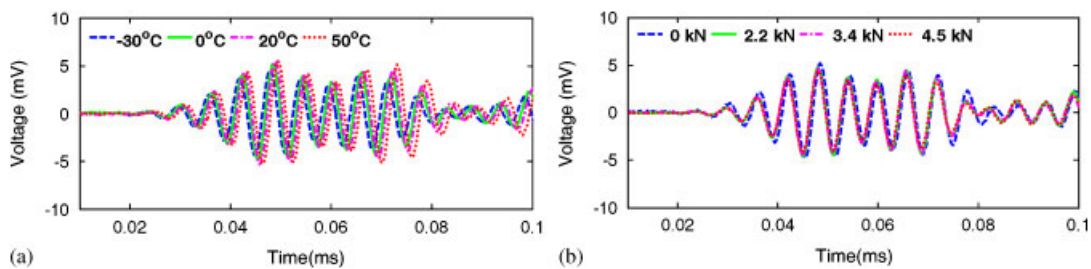


Figure 13. Variations of mode conversion signal  $D_{13}$  under changing temperature and loading conditions: (a) Under varying temperature and (b) Under varying loading levels

Next, damage diagnosis was repeated under varying loading conditions. A simple three-point loading test as shown in Figure 12(b) was performed under displacement control. To avoid the direct contact of the specimen with the UTM tip and the iron supports, rubber pads were inserted at these contact surfaces. Lamb wave signals were collected when the midpoint displacement of the specimen was 10, 15, and 20 mm, respectively.

The loading forces corresponding to these displacements were calculated to be 2.2, 3.4, and 4.5 kN, respectively, considering the material properties, shape and boundary conditions of the specimen. Amplitude and velocity variations of the mode conversion signal were observed in Figure 13(b), and similar results were reported in the literature [17]. Similar to the temperature experiments, satisfactory damage classification results are reported in Table I for the varying loading cases. In this study, the loading was controlled so that the maximum strain within the specimen would stay within an elastic range. In practice, excessive strain can lead to the performance deterioration of the PZTs and even cause PZT defects.

## 5. CONCLUSIONS

This study develops a new reference-free crack detection technique that utilizes specially designed PZTs placed on a single surface of a structure to detect crack damage in a plate-like structure. The basic premise of the proposed technique is that the mode conversion induced by a crack can be extracted from various signal pairs measured by the newly designed PZTs, and the mode conversion exceeding an instantaneously established threshold can be detected by exploiting the superposition relationships among measured signals. The proposed technique can

Table I. Reference-free damage diagnosis under temperature and external loading variations.

Case	Temp. (°C)	Energy ( $\times 10^{-4}$ )		Damage diagnosis	Load (kN)	Energy ( $\times 10^{-4}$ )		Damage diagnosis
		Threshold	AMCE			Threshold	AMCE	
Intact	−30	<b>10.9</b>	7.56	Intact	0	<b>10.1</b>	6.93	Intact
	0	<b>11.9</b>	6.93	Intact	2.2	<b>8.82</b>	7.91	Intact
	20	<b>12.7</b>	6.31	Intact	3.4	<b>8.56</b>	7.19	Intact
	50	<b>13.4</b>	6.12	Intact	4.5	<b>8.53</b>	7.22	Intact
Damage case I	−30	10.9	<b>18.8</b>	Damage	0	12.0	<b>18.3</b>	Damage
	0	12.0	<b>18.3</b>	Damage	2.2	9.15	<b>19.6</b>	Damage
	20	13.0	<b>17.1</b>	Damage	3.4	8.88	<b>19.0</b>	Damage
	50	13.8	<b>14.6</b>	Damage	4.5	8.63	<b>17.7</b>	Damage
Damage case II	−30	11.9	<b>18.6</b>	Damage	0	9.92	<b>13.2</b>	Damage
	0	11.9	<b>17.2</b>	Damage	2.2	9.36	<b>12.9</b>	Damage
	20	12.9	<b>17.4</b>	Damage	3.4	8.82	<b>12.0</b>	Damage
	50	15.7	<b>17.8</b>	Damage	4.5	9.94	<b>12.5</b>	Damage

The bold value under 'Energy' column denotes the bigger value between threshold and AMCE.

detect cracks even when measured Lamb wave time signals are complex due to the existence of multiple modes and reflections, overcoming the limitation of the previous reference-free techniques in the time domain. Moreover, the data collection time has been significantly reduced by allowing the use of broadband chirp input waveforms and narrowband toneburst signals. The instantaneous threshold for damage classification is established using the signals acquired only from the current condition of the structure. Finally, the robustness of the proposed technique against not only temperature changes but also varying external static loading is verified. However, the application of the current technique is limited only to plate structures with uniform thickness. Future work is warranted to extend its applications to more complex structures, such as steel bridges, aircraft, and pipelines.

#### ACKNOWLEDGEMENTS

This work is supported by the Radiation Technology Program (M20703000015-07N0300-01510) and the Nuclear Research & Development Program (2009-0083489) of National Research Foundation of Korea (NRF) funded by Ministry of Education, Science & Technology (MEST). Any opinions, findings, and conclusions or recommendations expressed in this material are those of the author(s) and do not necessarily reflect the views of the funding agencies.

#### REFERENCES

1. Raghavan A, Cesnik CES. Review of guided-wave structural health monitoring. *Shock and Vibration Digest* 2007; **39**(2):91–114.
2. Cawley P, Alleyne D. The use of Lamb waves for the long range inspection of large structures. *Ultrasonics* 1996; **34**(2–5):287–290.
3. Ghosh T, Kundu T, Karpur P. Efficient use of Lamb modes for detecting defects in large plates. *Ultrasonics* 1998; **36**(7):791–801.

4. Rose J. A baseline and vision of ultrasonic guided wave inspection potential. *Journal of Pressure Vessel Technology, Transactions of the ASME* 2002; **124**(3):273–282.
5. Ihn JB, Chang FK. Detection and monitoring of hidden fatigue crack growth using a built-in piezoelectric sensor/actuator network: I. Diagnostics. *Smart Materials and Structures* 2004; **13**(3):609–620.
6. Sohn H. Effects of environmental and operational variability on structural health monitoring. *Philosophical Transactions of the Royal Society A* 2007; **365**(1851):539–560.
7. Kim S B, Sohn H. Instantaneous reference-free crack detection based on polarization characteristics of piezoelectric materials. *Smart Materials and Structures* 2007; **16**(6):2375–2387.
8. Kim S B, Sohn H. Instantaneous crack detection using dual-PZT transducers. *Proceedings of SPIE-The International Society for Optic Engineering* 2008; 693509.
9. Available from: <http://www.metisdesign.com>.
10. Viktorov I. *Rayleigh and Lamb Waves*. Plenum Press: New York, 1967.
11. Cho Y. Estimation of ultrasonic guided wave mode conversion in a plate with thickness variation. *IEEE Transactions on Ultrasonics, Ferroelectrics and Frequency Control* 2000; **47**(3):591–603.
12. Raghavan A, Cesnik CES. Finite-dimensional piezoelectric transducer modeling for guided wave based structural health monitoring. *Smart Materials and Structures* 2005; **14**(6):1448–1461.
13. Sohn H, Lee SJ. Lamb wave tuning curve calibration for surface-bonded pzt transducers. *Smart Materials and Structures* 2010; **19**(1):015007.
14. Park HW, Sohn H. Parameter estimation of the generalized extreme value distribution for structural health monitoring. *Journal of Probabilistic Engineering Mechanics* 2006; **21**(4):366–376.
15. COMSOL AB. COMSOL Multiphysics User's Guide, 2005.
16. Kim SB, Sohn H. Application of time reversal guided waves to field bridge testing for baseline free damage diagnosis. *Proceedings of SPIE-The Int'l Society for Optical Engineering* 2006; Art. No. 617703.
17. Chen F, Wilcox PD. The effect of load on guided wave propagation. *Ultrasonics* 2007; **47**(1–4):111–122.